

SCIENTIFIC REPORTS

OPEN

High conductivity of ultrathin nanoribbons of SrRuO₃ on SrTiO₃ probed by infrared spectroscopy

E. Falsetti¹, A. Kalaboukhov², A. Nucara³, M. Ortolani¹, M. Corasaniti¹, L. Baldassarre¹, P. Roy⁴ & P. Calvani³

SrRuO₃ (SRO) is a perovskite increasingly used in oxide-based electronics both for its intrinsic metallicity, which remains unaltered in thin films and for the ease of deposition on dielectric perovskites like SrTiO₃, (STO) to implement SRO/STO microcapacitors and other devices. In order to test the reliability of SRO/STO also as high-current on-chip conductor, when the SRO dimensions are pushed to the nanoscale, here we have measured the electrodynamic properties of arrays of nanoribbons, fabricated by lithography starting from an ultrathin film of SRO deposited on a STO substrate. The nanoribbons are 6 or 4 nm thick, 400, 200 and 100 nm wide and 5 mm long. The measurements have been performed by infrared spectroscopy, a non-contact weakly perturbing technique which also allows one to separately determine the carrier density and their scattering rate or mobility. Far-infrared reflectivity spectra have been analyzed by Rigorous Coupled-Wave Analysis (RCWA) and by an Effective Medium Theory, obtaining consistent results. With the radiation polarized along the nanoribbons, we obtain a carrier density similar to that of a flat film used as reference, which in turn is similar to that of bulk SRO. Moreover, in the nanoribbons the carrier scattering rate is even smaller than in the unpatterned film by about a factor of 2. This shows that the transport properties of SRO deposited on STO remain at least unaltered down to nanometric dimensions, with interesting perspectives for implementing on-chip nano-interconnects in an oxide-based electronics. When excited in the perpendicular direction, the nanoribbons appear instead virtually transparent to the radiation field, as predicted by RCWA.

SrRuO₃ (SRO) is a perovskite which, like other strontium ruthenates of the Ruddlesden-Popper series Sr_{n+1}Ru_nO_{3n+1} (where the SRO formula is obtained for $n = \infty$), displays intrinsic metallic conductivity, even if a true Fermi liquid behavior is reported only at low temperature^{1–3} and itinerant ferromagnetism appears below about 160 K. At 300 K the dc resistivity of a SRO film 100 nm thick is⁴ 200 μΩcm, a low value for a perovskitic oxide. Its high chemical stability and thermal conductivity, the absence of dopant impurities and the good structural compatibility with substrates like NdGaO₃, LaAlO₃ and SrTiO₃ (STO), make the growth of SRO thin films easier than for many other conducting perovskites. Another advantage is that the physical properties of SRO thin films are very similar to those of bulk samples⁵. All these properties have been exploited to implement efficient SRO electrodes for complex oxide heterostructures, like microcapacitors⁶, Josephson junctions⁷ and Schottky junctions⁸, while interesting perspectives are opening for plasmonic applications⁹. Few years ago, the possibility to pattern SRO samples at the nanoscale has been demonstrated by growing nanowires 100 nm wide, 5–10 nm thick and at least 25 μm long, on suitably terminated DyScO₃ substrates.

Here, we have produced arrays of parallel and straight SRO nanoribbons on STO, 6 or 4 nm thick, 400, 200 and 100 nm wide and 5 mm long, by lithographic techniques¹⁰. We have then performed reflectivity measurements with radiation polarized either along the ribbons or orthogonal to them, from the far to the near infrared and at temperatures from 300 to 6 K. Infrared spectroscopy is indeed a powerful tool to investigate the electrodynamic properties of solids with high sensitivity, low perturbation and no need for contacts. The optical response of SRO

¹Dipartimento di Fisica, Università di Roma “La Sapienza”, P.le A. Moro 2, I-00185, Roma, Italy. ²Department of Microtechnology & Nanoscience, Chalmers University, S-41296, Gothenburg, Sweden. ³CNR-SPIN and Dipartimento di Fisica, Università di Roma “La Sapienza”, P.le A. Moro 2, I-00185, Roma, Italy. ⁴Synchrotron SOLEIL, L’Orme des Merisiers Saint-Aubin, BP 48, F-91192, Gif-sur-Yvette Cedex, France. Correspondence and requests for materials should be addressed to A.N. (email: alessandro.nucara@roma1.infn.it)

unpatterned films was previously investigated in the THz range by Dodge *et al.*¹¹ and, in the infrared domain, by Kostic *et al.*¹². In the latter experiment the film was 420 nm thick. Here, by a Rigorous Coupled Wave Analysis (RCWA) of our reflectivity spectra, we were able to determine the plasma frequency ω_p and the scattering rate γ_D of the carriers in the nanoribbons, thus obtaining also their charge density n and mobility μ . The former quantity is similar to that measured in a flat SRO film, 6 nm thick, used as reference, while μ is even better than in the unpatterned film, by about a factor of 2.

Four SrRuO₃ films A, B, C and D were deposited on crystalline SrTiO₃ substrates, TiO₂ terminated, 5 × 5 mm wide, by Pulsed Laser Deposition (PLD). They were then annealed under 5 × 10⁻² mbar O₂ at 750 °C and structurally characterized as previously described in reference¹³ for the growth of LaAlO₃ films on STO. The thickness d of A, B and D was 6 nm (10 u. c.), that of C 4 nm. Shortly after growth, dc-resistance and Hall measurements were performed on the 6 nm thick sample B before nano-patterning. The measurements were performed in the Van der Pauw geometry¹⁴ under a magnetic field $H = 5$ T applied in the direction perpendicular to the film plane. The resulting, in-plane Hall resistance R_{xy} , is reported vs. temperature and normalized to H , in panel d of Fig. 1. The in-plane resistivity ρ , shown in the inset of the same panel, displays a good metallic behavior vs. temperature and the usual change of slope (indicated by an arrow in the inset of Fig. 1d) at the ferromagnetic transition¹⁵. This occurs around 140 K, a T_c value rather high for an ultrathin film^{16,17}, while the ρ value at 300 K (575 $\mu\Omega\text{cm}$) is comparable with those in the literature for SRO/STO films of similar thickness¹⁸. In turn, R_{xy} changes sign below the ferromagnetic transition. The Hall effect in the ferromagnetic state of SrRuO₃ consists of two contributions: the ordinary Hall effect related to the carrier concentration and the anomalous Hall effect that depends on the sample magnetization⁵. The latter contribution has been mainly attributed either to an extrinsic mechanism of spin-dependent preferred scattering¹⁹, or to an intrinsic Berry-phase mechanism²⁰. In both cases, the behavior of the Hall resistance depends on the applied magnetic field and on the magnetization direction of the sample. Therefore, one cannot obtain a straightforward determination of the carrier concentration from the Hall coefficient alone in SrRuO₃. Given the above problems, an infrared determination of this parameter will then be particularly meaningful and useful.

After growth, samples B, C and D were covered by a mask in form of thin stripes and exposed to an Ar⁺ beam¹³ for 5 minutes at a beam energy of 150 eV, in order to etch the SRO film along parallel ribbons, 5 mm long, having different widths W and period $2W$. Film A was instead kept as grown, to be used as reference. The widths W of the conducting nanoribbons in the atomic-force microscope (AFM) images of Fig. 1 were 400 nm, 200 nm and 100 nm for B, C and D, respectively and their period was always $2W$. In panels a–c of Fig. 1 the ribbon profiles are also shown.

The samples were mounted on the cold finger of a He-flow cryostat. The reference was a gold mirror placed above the sample and aligned parallel to it by a laser beam. Unpolarized radiation was extracted from a global source and modulated by a commercial, Bruker 66 V, Michelson interferometer. Infrared radiation could illuminate either the sample or the mirror at exactly normal incidence, by use of a home-made reflectivity setup based on a beamsplitter and a parabolic mirror. The incident radiation passed through a wire-grid polarizer that could be remotely rotated and the reflected radiation was collected by a liquid-helium cooled bolometer in the far infrared, by a nitrogen-cooled Mercury-Cadmium-Tellurium detector in the mid infrared. The reflectivities $R_{\parallel}(\omega)$ and $R_{\perp}(\omega)$, as measured with the electric field parallel and orthogonal to the stripes, respectively, were thus obtained. In a preliminary experiment, $R_{\parallel}(\omega)$ and $R_{\perp}(\omega)$ were measured on the uniform sample A to check that they were identical (see Fig. 2). They were then fit by employing the usual formulas for a three-layer system^{21,22} (vacuum-SRO-STO) where one uses the Drude-Lorentz dielectric functions

$$\tilde{\epsilon}_{\text{SRO}} = \epsilon_{\infty} - \frac{\omega_p^2}{\omega^2 + i\gamma_D\omega} \quad (1)$$

and

$$\tilde{\epsilon}_{\text{STO}} = \epsilon_{\infty} \left(\prod_{j=1}^n \frac{\omega_{L,j}^2 - \omega^2 - i\Gamma_{L,j}\omega}{\omega_{T,j}^2 - \omega^2 - i\Gamma_{T,j}\omega} \right) \quad (2)$$

Therein, ω_p is the plasma frequency of SRO, γ_D the carrier scattering rate, $\omega_{L,j}$ and $\omega_{T,j}$ are the longitudinal and transverse phonon frequencies of STO, respectively. $\Gamma_{L,j}$ and $\Gamma_{T,j}$ are the corresponding linewidths. The Drude parameters of sample A are listed in Table 1. One may notice that our γ_D at 300 K is in excellent agreement with that reported by Kostic *et al.*¹² (in a SRO film 70 times thicker), who assume a frequency dependent scattering rate varying between 1700 and 2200 cm⁻¹ in the far-infrared range at 250 K. From those formulas one can easily obtain the real part σ_1 of the optical conductivity shown in the inset of Fig. 3, which in a first approximation displays a conventional Drude term. Its extrapolation for $\omega \rightarrow 0$ provides a σ_{dc} close to 4000 $\Omega^{-1}\text{cm}^{-1}$, again in excellent agreement with the result of reference¹². Moreover, considering the entirely different techniques by which the two measurements have been made, this value is also in satisfactory agreement with the directly measured dc value in panel (d) of Fig. 1 (about 2000 $\Omega^{-1}\text{cm}^{-1}$).

The reflectivities $R_{\parallel}(\omega)$ and $R_{\perp}(\omega)$ of the three patterned samples are shown instead in Fig. 3, at both the highest and lowest temperature. $R_{\parallel}(\omega)$ is similar to that observed in the homogeneous sample A, while $R_{\perp}(\omega)$ resembles that of the bare STO substrate. In order to extract the Drude parameters of the nanoribbons from $R_{\parallel}(\omega)$, the reflectivity has been simulated by a Rigorous Coupled Wave Analysis (RCWA). This semi-analytical method has been proven to be a powerful tool for modeling multilayer and periodic structures²³ and has been successfully used to analyze THz and infrared data^{24–26}. In the present case, the nanoribbon profile has been expanded up to

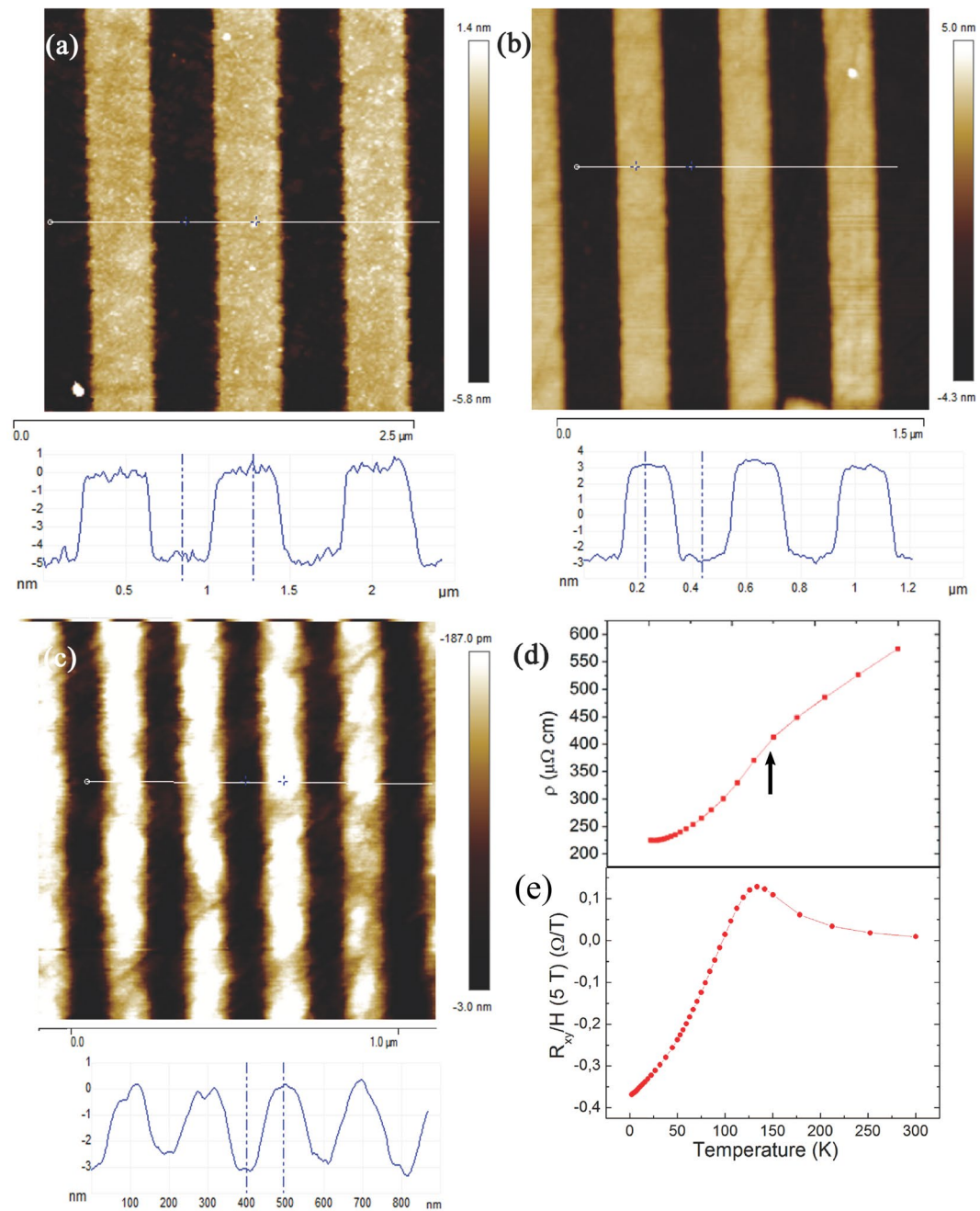


Figure 1. (a–c) AFM images of the SRO/STO samples B, C ($d = 6$ nm) and D ($d = 4$ nm), showing their conducting nanoribbons (brighter) of widths $W = 400$, 200 and $= 100$ nm, respectively, spaced by insulating wires (darker). The corresponding AFM height profile is reported under each image. (d) Temperature dependence of the dc resistivity and of the Hall resistance (e) in sample B before Ar ion etching. The arrow indicates the T_c of the ferromagnetic transition in the SRO film.

the 15th Fourier component, while the incident radiation has been developed in plane waves with frequencies differing by 1 cm^{-1} from each other, in the range 100 to 950 cm^{-1} . Then, the reflectivity is obtained by calculating the eigenmodes of both the electric and magnetic fields in each layer. The problem is finally solved by matching the boundary conditions at each interface with scattering matrices (SM). We have adapted a previously known code²⁷ which implements the RCWA-SM based on the formalism used in references^{28–31} and takes into account the dispersion characteristics of the media involved. The simulated curves obtained with this method are in good agreement with the measured reflectivity of all patterned SRO/STO samples, using the STO phonon spectrum measured in a previous experiment³² and, for SRO, Drude parameters not too different from those of the flat film.

The best agreement with the experimental data is found for the plasma frequencies and scattering rates reported in Table 1 for the radiation field parallel to the ribbons at two temperatures and the corresponding curves are shown together with the measured spectra in Fig. 3. The best simulation has also provided the real part

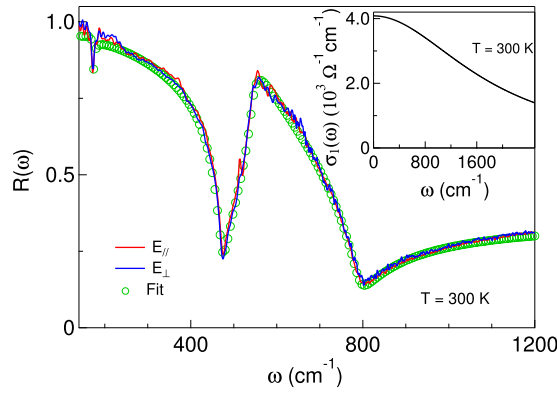


Figure 2. Reflectance measured at 300 K on the SRO/STO unpatterned sample A, having a SRO thickness $d = 6$ nm, in the same two polarizations that were then used on the striped samples B, C and D (red and blue curves). The open circles show the fit to reflectivity data described in the text, which provides the real part σ_1 of the optical conductivity displayed in the inset.

Sample	d (nm)	W (nm)	ω_p, γ_D (300 K)	ω_p, γ_D (100 K)	ω_p, γ_D (6 K)
A	6	—	21000, 1800	—	—
[RCWA simulation]					
B	6	400	21000, 800	18500, 600	19000, 600
C	6	200	23000, 850	22000, 550	21000, 600
D	4	100	16000, 950	15000, 750	14000, 850
[EMT fits]					
B	6	400	19500, 810	18000, 670	19000, 560
C	6	200	23000, 820	23600, 630	23000, 630
D	4	100	13000, 600	16000, 680	15500, 800

Table 1. Plasma frequencies ω_p and scattering rates γ_D at three temperatures, in cm^{-1} , of the nanoribbons as obtained by the RCWA simulation and by Effective Medium Theory (EMT) fits.

σ_1 of the optical conductivity of the SRO nanoribbons at 300 and 6 K, shown in Fig. 4. The conductivity is that of a conventional Drude term, which for $\omega \rightarrow 0$ extrapolates to $\sigma_{dc} \sim 10^4 \Omega^{-1} \text{cm}^{-1}$ for the wider nanoribbons, to about a half of that value for the 100 nm wide ribbon. One may notice that the former value is higher than in the unpatterned film A, thanks to the smaller scattering rate measured in the ribbons, while σ_{dc} for the 100 nm sample D is similar to that of A, despite a smaller γ_D , due to its reduced charge density. This decrease can be tentatively attributed either to the presence of a dead layer at the interface, here more effective than in the other films due to the lower thickness of D (4 nm), or to the effect of ion etching which, in the narrowest ribbon, may have partially damaged also the conducting stripes.

Table 1 also shows that, within a 10% incertitude on the fitting parameters, the Drude plasma frequency ω_p does not vary significantly with temperature, as expected for a metallic behavior. Similarly, it does not change appreciably when passing from the unpatterned SRO film A to the nanoribbons B and C. In turn, interestingly, the carrier scattering rate γ_D , in all nanoribbons, is smaller than in the flat film by about a factor of 2. A similar conductivity enhancement was observed in a nanopatterned quasi-two-dimensional electron system (q-2DES) at the interface between^{13,33} LaAlO_3 and SrTiO_3 . Its origin is still unclear and deserves further investigation. In any case, the present experiment demonstrates that the SRO metallic properties are quite well conserved in nanoribbons a few nm thick (10–15 monolayers) and down to 100 nm wide.

As a further control on the RCWA results, we have also fitted to our reflectivity data a conventional Effective Medium Theory (EMT), where the permittivity of the striped samples is written, for $W \ll \lambda$, as

$$\tilde{\epsilon}_{eff,||} = f\tilde{\epsilon}_{SRO} + (1-f)\epsilon_0 \quad (3)$$

$$\tilde{\epsilon}_{eff,\perp} = \frac{\epsilon_0 \tilde{\epsilon}_{SRO}}{f\epsilon_0 + (1-f)\tilde{\epsilon}_{SRO}} \quad (4)$$

Therein, f is the filling factor (nominal value 0.5) and ϵ_0 is the permittivity of a vacuum. The fitting procedure, which continues by use of Eqs 1 and 2 and of the three-layer optical formulas²¹, provides the lines which in Fig. 5 are compared with the raw data and with the RCWA simulation. A similar agreement was obtained for samples C and D. The Drude parameters thus obtained are compared in Table 2 at three temperatures. The filling factor was left as a free parameter and turned out to be 0.48 ± 0.01 for all samples at all temperatures. As one can see, both

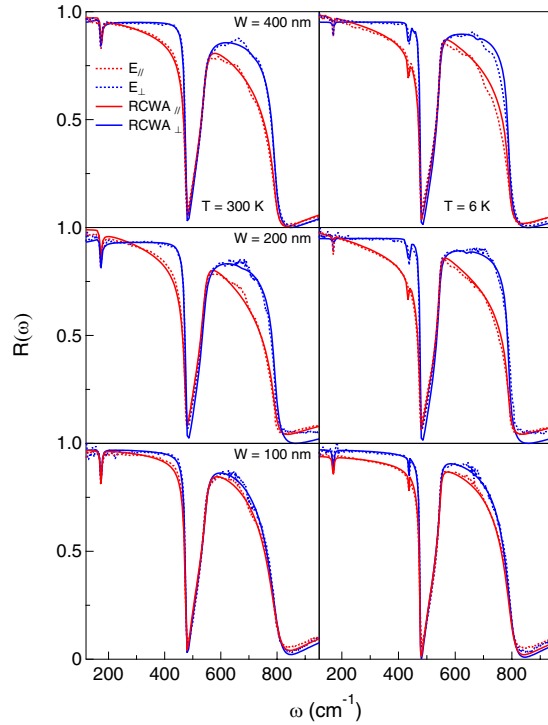


Figure 3. Reflectance measured at 100 K on the SRO/STO samples B, C and D, from top to bottom, with the corresponding simulations performed with the RCWA approach (see text).

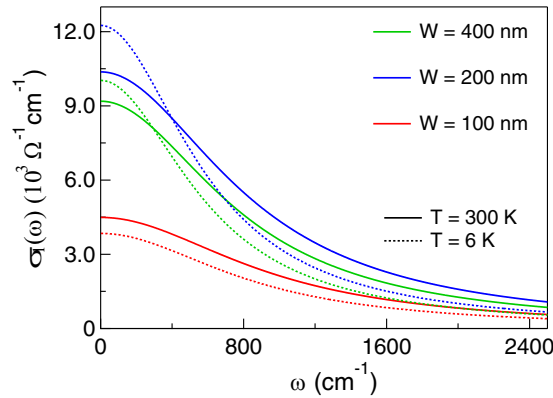


Figure 4. Real part σ_1 of the optical conductivity at 300 and 6 K measured on the nanoribbons B, C and D, from top to bottom, as obtained from the reflectivities in Fig. 3 by RCWA (see text).

approaches provide fits of excellent quality and two sets of Drude parameters which are fully consistent with each other, even if the RCWA approach looks more suitable to the pattern geometry of the present samples.

When turning the polarization in the direction orthogonal to the stripes, as already mentioned $R_{\perp}(\omega)$ appears very similar to that of bare STO³² in all panels of Fig. 3. Indeed, when the charges are excited orthogonally to the nanometric ribbons, the SRO Drude term (which in the parallel polarization partially screens the STO optical phonons) should be replaced by a surface plasmon-polariton (SPP) of wavevector $k = \pi/W$, peaked at a finite frequency given by³²

$$\omega_{spp} = \sqrt{\frac{e^2 N_{2D} \pi}{m^* \bar{\epsilon}_{\infty} W}} = \omega_p \sqrt{\frac{d}{4 \bar{\epsilon}_{\infty} W}} \quad (5)$$

where $N_{2D} = n \cdot d$ is the surface charge density, $m^* = 4.1 m_e$ ³⁴ is the carrier effective mass and $\bar{\epsilon}_{\infty}$ is averaged over the high-frequency permittivities of SRO and STO. Such plasmonic excitations have been detected, for example, in the two-dimensional electron systems (2DES) of graphene³⁵ and topological insulators³⁶ using patterned surfaces. Here, by introducing in Eq. 5 the values of W , d and ω_p from Table 1 and $\bar{\epsilon}_{\infty} = 3.4$, one obtains $\omega_{spp} = 670$, 940 and 790 cm^{-1} for samples B, C and D, respectively. However, the weak SPP absorption could not be detected

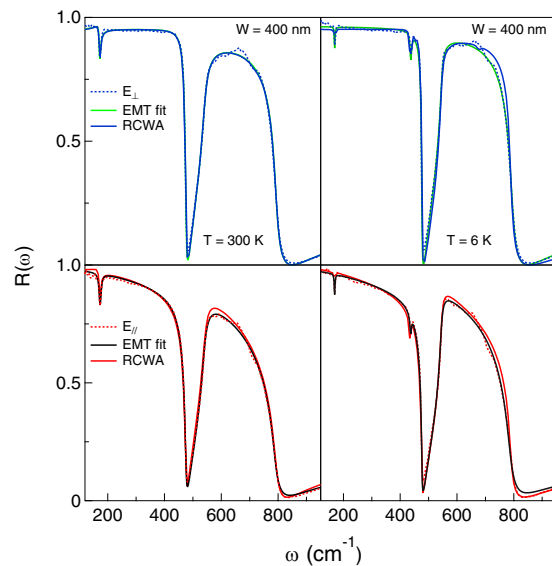


Figure 5. Comparison between the fit to data obtained by the Effective Medium Theory approach and the RCWA simulation for sample B at two temperatures in both polarizations.

Sample	n (300 K)	μ (300 K)	n (100 K)	μ (100 K)	n (6 K)	μ (6 K)
A	2.0×10^{22}	1.3	—	—	—	—
B	1.9×10^{22}	2.9	1.6×10^{22}	3.9	1.6×10^{22}	3.9
C	2.0×10^{22}	2.8	1.9×10^{22}	4.2	1.9×10^{22}	3.9
D	1.1×10^{22}	2.5	9.3×10^{21}	3.1	8.7×10^{21}	2.8

Table 2. Volume charge density n in cm^{-3} and mobility μ in cm^2/Vs , as extracted from the ω_p and γ_D in Table 1 for samples B, C and D (RCWA simulation), at three temperatures. The same parameters are reported for sample A at 300 K, as obtained from Drude-Lorentz fits for a three-layer system as explained in the text.

in the present experiment, probably for the presence of the strong infrared-active STO phonons that damp plasmonic oscillations decreasing their lifetime and increasing their spectral linewidth. This adds to the high value of γ_D , which should reflect in a very broad SPP lineshape. Finally, due to the high reflectivity of the bare STO substrate in the far infrared, the changes in the sample $R_{\perp}(\omega)$ are expected to be weak anyway. As a result, the SRO film is virtually transparent to the far-infrared radiation and $R_{\perp}(\omega)$ reproduces approximately that of the underlying STO.

In conclusion, we have studied the conducting properties of SrRuO₃ ultrathin nanoribbons on SrTiO₃, few hundreds of nanometers wide and of macroscopic length, to test their reliability as on-chip interconnects for an oxide-based electronics. The measurements have been performed by infrared spectroscopy, a non-contact weakly perturbing technique which also allows one to separately determine the density of carriers and their scattering rate or mobility. Data have then been analyzed by Rigorous Coupled-Wave Analysis and Effective Medium Theory, with the two methods providing fully consistent results. With the radiation polarized along the nanoribbons, we have obtained a carrier density similar to that of a flat film of similar thickness that we used as reference, whose conductivity is in turn very similar to that reported in the literature for much thicker SRO films. Moreover, in the nanoribbons the carrier scattering rate is even smaller than in the unpatterned film by about a factor of 2. This shows that the transport properties of SRO deposited on STO remain unaltered down to nanometric dimensions, with interesting perspectives for an oxide-based electronics. When excited in the perpendicular direction, the nanoribbons appear instead virtually transparent to the radiation field, as expected and predicted by RCWA.

Data Availability

The datasets generated during the current study are available from the corresponding author on reasonable request.

References

- Mackenzie, A. P. *et al.* Observation of quantum oscillations in the electrical resistivity of SrRuO₃. *Phys. Rev. B* **58**, R13318–R13321 (1998).
- Kaur, P., Sharma, K. K., Pandit, R., Choudhary, R. J. & Kumar, R. Structural, electrical and magnetic properties of SrRuO₃ thin films. *Appl. Phys. Lett.* **104**, 081608–081612 (2014).
- Majcher, A. M., Rode, K., Coey, J. M. D. & Stamenov, P. Magnetic, transport and structural properties of SrRuO₃ thin films. *J. Appl. Phys.* **115**, 179901–179904 (2014).

4. Vailionis, A., Siemons, W. & Koster, G. Strain-induced single-domain growth of epitaxial SrRuO₃ layers on SrTiO₃: A high temperature x-ray diffraction study. *Appl. Phys. Lett.* **91**, 071907–071909 (2007).
5. Koster, G. *et al.* Structure, physical properties and applications of SrRuO₃ thin films. *Rev. Mod. Phys.* **84**, 253–298 (2012).
6. Eom, C. B. *et al.* Single-crystal epitaxial thin films of the isotropic metallic oxides Sr_{1-x}Ca_xRuO₃ (0 < x < 1). *Science* **258**, 1766–1769 (1992).
7. Gausepohl, S. C., Lee, M., Antognazza, L. & Char, K. Magnetoresistance probe of spatial current variations in highT_c YBa₂Cu₃O₇/SrRuO₃/YBa₂Cu₃O₇ Josephson junctions. *Appl. Phys. Lett.* **67**, 1313–1315 (1995).
8. Fujii, T. *et al.* Hysteretic current-voltage characteristics and resistance switching at an epitaxial oxide Schottky junction SrRuO₃/SrTi_{0.99}Nb_{0.01}O₃. *Appl. Phys. Lett.* **86**, 012107–012109 (2005).
9. Braic, L. *et al.* Optimizing strontium ruthenate thin films for near-infrared plasmonic applications. *Sci. Rep.* **5**, 9118–9122 (2015).
10. Kuiper, B. *et al.* Self-organization of SrRuO₃ nanowires on ordered oxide surface terminations. *MRS Commun.* **1**, 17–21 (2011).
11. Dodge, J. S. *et al.* Low-frequency crossover of the fractional power-law conductivity in SrRuO₃. *Phys. Rev. Lett.* **85**, 4932–4935 (2000).
12. Kostic, P. *et al.* Non-Fermi-liquid behavior of SrRuO₃: evidence from infrared conductivity. *Phys. Rev. Lett.* **81**, 2498–2501 (1998).
13. Aurino, P. P. *et al.* Nano-patterning of the electron gas at the LaAlO₃/SrTiO₃ interface using low-energy ion beam irradiation. *Appl. Phys. Lett.* **102**, 201610–201613 (2013).
14. van der Pauw, J. L. A method of measuring specific resistivity and hall effect of disks of arbitrary shape. *Philips Res. Rep.* **13**, 1–9 (1958).
15. Klein, L. *et al.* Transport and magnetization in the badly metallic itinerant ferromagnet SrRuO₃. *J. Phys. Condens. Matter* **8**, 10111–10126 (1996).
16. Toyota, D., Ohkubo, I., Kumigashira, H. & Oshima, M. Ferromagnetism stabilization of ultrathin SrRuO₃ films: thickness-dependent physical properties. *J. Appl. Phys.* **99**, 08N505–08N507 (2006).
17. Kats, Y., Genish, I., Klein, L., Reiner, J. W. & Beasley, M. R. Large anisotropy in the paramagnetic susceptibility of SrRuO₃ films. *Phys. Rev. B* **71**, 100403–100406 (2005).
18. Schultz, M., Levy, S., Reiner, J. W. & Klein, L. Magnetic and transport properties of epitaxial films of SrRuO₃ in the ultrathin limit. *Phys. Rev. B* **79**, 125444–125449 (2009).
19. Kats, Y., Genish, I., Klein, L., Reiner, J. W. & Beasley, M. R. Testing the Berry phase model for extraordinary Hall effect in SrRuO₃. *Phys. Rev. B* **70**, R180407–R180409 (2004).
20. Mathieu, R. *et al.* Scaling of the anomalous Hall effect in Sr_{1-x}Ca_xRuO₃. *Phys. Rev. Lett.* **93**, 016602–016605 (2004).
21. Dressel, M. & Grüner, G. *Electrodynamics of solids* (Cambridge Univ. Press, 2002).
22. Nucara, A. *et al.* Infrared study of the quasi-two-dimensional electron system at the interface between SrTiO₃ and crystalline or amorphous LaAlO₃. *Phys. Rev. B* **97**, 155126–155132 (2018).
23. Moharam, M. G. & Gaylord, T. K. Rigorous coupled-wave analysis of planar-grating diffraction. *J. Opt. Soc. Am.* **71**, 811–818 (1981).
24. Kreilkamp, L. E. *et al.* Terahertz dynamics of lattice vibrations in Au/CdTe plasmonic crystals: Photoinduced segregation of Te and enhancement of optical response. *Phys. Rev. B* **93**, 125404–125413 (2015).
25. Zang, X. *et al.* Ultra-broadband terahertz absorption by exciting the orthogonal diffraction in dumbbell-shaped gratings. *Scientific Reports* **5**, 8901–8905 (2015).
26. Streyer, W., Feng, K., Zhong, Y., Hoffman, A. J. & Wasserman, D. Selective absorbers and thermal emitters for far-infrared wavelengths. *Appl. Phys. Lett.* **107**, 081105–081109 (2015).
27. Zannotto, S. Electromagnetic properties of patterned multilayers based on RCWA (Rigorous Coupled Wave Analysis), <https://www.mathworks.com/matlabcentral/fileexchange/55401-ppml-periodically-patterned-multi-layer> (2016).
28. Whittaker, M. & Culshaw, I. S. Scattering-matrix treatment of patterned multilayer photonic structures. *Phys. Rev. B* **60**, 2610–2618 (1999).
29. Liscidini, M., Gerace, D., Andreani, L. C. & Sipe, J. E. Scattering-matrix analysis of periodically patterned multilayers with asymmetric unit cells and birefringent media. *Phys. Rev. B* **77**, 035324–035334 (2008).
30. Li, L. Use of Fourier series in the analysis of discontinuous periodic structures. *J. Opt. Soc. Am. A* **13**, 1870–1876 (1996).
31. Lalanne, P. & Morris, G. M. Highly improved convergence of the coupled-wave method for TM polarization. *J. Opt. Soc. Am. A* **13**, 779–784 (1996).
32. Nucara, A. *et al.* Hardening of the soft phonon in bulk SrTiO₃ interfaced with LaAlO₃ and SrRuO₃. *Phys. Rev. B* **93**, 224103–224109 (2016).
33. Irvin, P. *et al.* Anomalous high mobility in LaAlO₃/SrTiO₃ nanowires. *Nanolett.* **13**, 364–368 (2013).
34. Siemons, W. *et al.* Dependence of the electronic structure of SrRuO₃ and its degree of correlation on cation off-stoichiometry. *Phys. Rev. B* **76**, 075126–075131 (2007).
35. Ju, L. *et al.* Graphene plasmonics for tunable terahertz metamaterials. *Nature Nanotech.* **6**, 630–634 (2011).
36. Di Pietro, P. *et al.* Observation of Dirac plasmons in a topological insulator. *Nature Nanotech.* **8**, 556–560 (2013).

Acknowledgements

This work has been partially supported by the Italian Ministry of University and Research through the PRIN project *OXIDE* and by the funds Ateneo 2016 of the Sapienza University of Rome. We also acknowledge SOLEIL for provision of beamtime under the Proposal 20170072 and we thank for assistance all personnel of the AILES beamline.

Author Contributions

The research was conceived by P.C. and E.F.; A.K. grown the films and performed Hall and resistivity measurements; A.N., M.O., L.B., E.F. and M.C. performed the infrared experiments; supervision and technical assistance to the experiments was provided by P.R. and P.C.; M.O., E.F. and A.N. performed the data analysis; P.C. drafted the manuscript. All Authors contributed to the final version of the manuscript.

Additional Information

Competing Interests: The authors declare no competing interests.

Publisher's note: Springer Nature remains neutral with regard to jurisdictional claims in published maps and institutional affiliations.



Open Access This article is licensed under a Creative Commons Attribution 4.0 International License, which permits use, sharing, adaptation, distribution and reproduction in any medium or format, as long as you give appropriate credit to the original author(s) and the source, provide a link to the Creative Commons license, and indicate if changes were made. The images or other third party material in this article are included in the article's Creative Commons license, unless indicated otherwise in a credit line to the material. If material is not included in the article's Creative Commons license and your intended use is not permitted by statutory regulation or exceeds the permitted use, you will need to obtain permission directly from the copyright holder. To view a copy of this license, visit <http://creativecommons.org/licenses/by/4.0/>.

© The Author(s) 2018